LUND UNIVERSITY

Maximum Gain, Effective Area, and Directivity

Gustafsson, Mats; Capek, Miloslav

2018

Link to publication

Citation for published version (APA):
Gustafsson, M., & Capek, M. (2018). *Maximum Gain, Effective Area, and Directivity*. Electromagnetic Theory Department of Electrical and Information Technology Lund University Sweden.

Total number of authors:
2

General rights
Unless other specific re-use rights are stated the following general rights apply:
Copyright and moral rights for the publications made accessible in the public portal are retained by the authors and/or other copyright owners and it is a condition of accessing publications that users recognise and abide by the legal requirements associated with these rights.
• Users may download and print one copy of any publication from the public portal for the purpose of private study or research.
• You may not further distribute the material or use it for any profit-making activity or commercial gain
• You may freely distribute the URL identifying the publication in the public portal

Read more about Creative commons licenses: https://creativecommons.org/licenses/

Take down policy
If you believe that this document breaches copyright please contact us providing details, and we will remove access to the work immediately and investigate your claim.

LUND UNIVERSITY

PO Box 117
221 00 Lund
+46 46-222 00 00

Download date: 10. Dec. 2025

CODEN:LUTEDX/(TEAT-7264)/1-28/(2018)

Maximum Gain, Effective Area, and Directivity

Mats Gustafsson and Miloslav Capek

Electromagnetic Theory
Department of Electrical and Information Technology
Lund University
Sweden

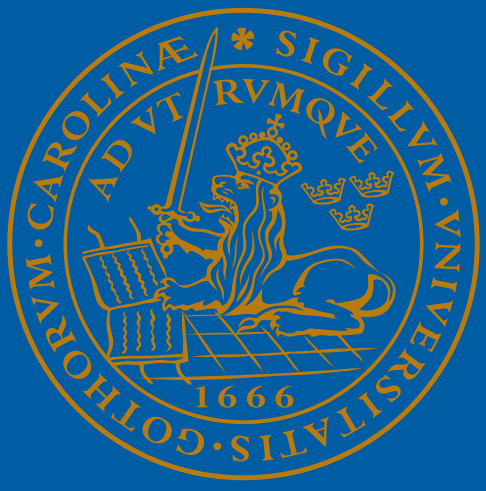

(TEAT-7264)/1-28/(2018): M. Gustafsson and M. Capek, Maximum Gain, Effective Area, and Directivity

Mats Gustafsson
mats.gustafsson@eit.lth.se

Department of Electrical and Information Technology
Electromagnetic Theory
Lund University
P.O. Box 118
SE-221 00 Lund
Sweden

Miloslav Capek
miloslav.capek@fel.cvut.cz

Department of Electromagnetic Field,
Faculty of Electrical Engineering,
Czech Technical University in Prague,
166 27 Prague,
Czech Republic

This is an author produced preprint version as part of a technical report series from the Electromagnetic Theory group at Lund University, Sweden. Homepage `http://www.eit.lth.se/teat`

Editor: Mats Gustafsson
© Mats Gustafsson and Miloslav Capek, Lund, December 11, 2018

Abstract

Fundamental bounds on antenna gain are found via convex optimization of the current density in a prescribed region. Various constraints are considered, including self-resonance and only partial control of the current distribution. Derived formulas are valid for arbitrarily shaped radiators of a given conductivity. All the optimization tasks are reduced to eigenvalue problems, which are solved efficiently. The second part of the paper deals with superdirectivity and its associated minimal costs in efficiency and Q-factor. The paper is accompanied with a series of examples practically demonstrating the relevance of the theoretical framework and entirely spanning wide range of material parameters and electrical sizes used in antenna technology. Presented results are analyzed from a perspective of effectively radiating modes. In contrast to a common approach utilizing spherical modes, the radiating modes of a given body are directly evaluated and analyzed here. All crucial mathematical steps are reviewed in the appendices, including a series of important subroutines to be considered making it possible to reduce the computational burden associated with the evaluation of electrically large structures and structures of high conductivity.

1 Introduction

A question of how narrow a radiation pattern can be or, in terms of standard antenna terminology [29], what are the bounds on directivity and gain, has been in the spotlight of antenna theorists' and physicists' for many years.

Early works studied needle-like radiation patterns [44]. A series of works starting in the 1940s revealed the fact that the directivity is unbounded [7] but also predicted the enormous cost in other antenna parameters, namely in Q-factor [25], related sensitivity of feeding network [60], and radiation efficiency in case that the antenna is made of lossy material [22]. Consequently, as pointed out by Hansen [21], the superdirective aperture design requires additional constraint, replacing fixed spacing in array theory [5, 57].

In order to tighten the bounds on directivity, Harrington [23, 25] proposed a simple formula which predicts the directivity from the number of used spherical harmonics as a function of aperture size. The number of modes radiating well and the pioneering works on bounds [24] became popular in antenna design and hold in many realistic cases, therefore, this approach demarcated the avenue of further research. Improved formula has been proposed in [35], suggesting that, in general, the maximum directivity in the electrically small region is equal to three. The maximum directivity is studied in [41] considering a given current norm. For antenna arrays, directivity bounds are shown in [52]. Trade-off between maximum directivity and Q-factor for arbitrarily shaped antennas is presented in [16]. Upper bounds for scattering of metamaterial-inspired structures are found in [40]. Recently, a composition of Huygens multipoles has been proposed [61] to increase the directivity. Notice, however, that no losses other than the radiation were assumed which re-opens the question of the actual cost of super-directivity.

Another way to limit the directional properties is a prescribed, non-zero, material resistivity of the antenna body [2, 33]. A quantity to deal with is the antenna gain, which is always bounded if at least infinitesimal losses are assumed. It may seem reasonable at this point to argue that the losses can be overcame with a concept of superconducting antennas, however, as shown in [22], the increase in gain with decrease of resistivity embodies slow (logarithmic) convergence. Consequently, even tiny losses, which are always present at RF, restrict the gain to a finite number.

Tightly connected is the question of maximum achievable absorption cross-section. The capability to effectively radiate energy in a certain direction can reciprocally be understood as a potential to absorb energy from that direction [13, 53]. This can be interpreted as an ability of a receiver to distort the near-field so that the incoming energy is effectively absorbed in the receiver's body or concentrated at the receiving port. It has been realized that such an area can be huge as compared to the physical size of the particle or the physical antenna aperture [6, 47]. Fundamental bounds on absorption cross-sections are proposed in [42, 54].

The importance to establish fundamental bounds on gain and absorption cross-section are underlined by recent development in design of superdirective (supergain) antennas and arrays [1, 11, 36, 39, 49, 59], partly fueled by the advent of novel materials and technologies [3, 14].

The procedure developed in this paper relies on convex optimization [8] of current distributions [16]. In order to find the optimal current distribution in a prescribed region, the antenna quantities are expressed as quadratic forms of corresponding matrix operators [17, 27]. This makes it possible to solve the optimization problems rigorously via eigenvalue problems [9, 15]. The procedure is general as arbitrarily shaped regions can be investigated. Additional constraints are enforced, *e.g.*, self-resonance and restricted controllability of the current [16, 30]. Much work in this area has already been done in determining bounds on Q-factor [9], radiation efficiency [30], superdirectivity [16], gain [24], and capacity [12]. The recent trend, followed by this paper, is to understand the mutual trade-offs between various parameters [15, 18, 32].

The original approach from [24] and [27] maximizing the Rayleigh quotient for antenna gain via a generalized eigenvalue problem is recast here into an eigenvalue problem of reduced rank. Such a formulation is compatible with fast numerical methods [10], therefore, the results can be presented in a wide frequency range, $ka \in [10^{-3}, 10^{3}]$, where ka is used throughout the paper to denote the dimensionless frequency with k being the wavenumber and a being the radius of a sphere circumscribing all the sources. The surface resistivity used spans the interval from extremely low values, $R_{\mathrm{s}} = 10^{-8}\ \Omega/\square$, reachable in RF superconducting cavities [45], through values valid for copper at RF ($R_{\mathrm{s}} \approx 0.01\ \Omega/\square$, $f = 1\,\mathrm{GHz}$), to poor conductors of surface resistivity $R_{\mathrm{s}} = 1\ \Omega/\square$.

Optimal currents presented in this paper maximize the antenna gain. Therefore, taking reciprocity into account, they delimit the maximum effective area of any receiver designed in that region as well. For this reason, the proportionality between gain and effective area is utilized, making it possible to judge the real performance of designed and manufactured antennas, arrays, scatterers, and other radiating sy-

stems.

The behavior of the optimal solution evolves markedly with electrical size. Huygens source formed by electric and magnetic dipoles is strictly preferred in electrically small (sub-wavelength) region and a large effect of self-resonance, if enforced, is observed. End-fire radiation and negligible effect of self-resonance constraint is observed in an intermediate region. Finally, broadside radiation dominates in the electrically large region with the effective area being proportional to the cross-section area.

The paper is organized as follows. Antenna gain and effective area are introduced in Section 2 and expressed as quadratic forms in the currents. The optimal currents are then found for maximum gain in Sections 2.1 and 2.2, including cases with additional constraints like self-resonance. Examples covering various aspects of antenna design are presented in Section 2.3. Superdirective currents are found in Section 3 and presented as a trade-off between required directivity and minimum ohmic losses or Q-factor. All presented examples reveal the enormous cost of superdirectivity. The maximum gain is reinterpreted in Section 4 in terms of number of sufficiently radiating modes of a structure and the results are linked back to Harrington's formula. The paper is concluded in Section 5. All required mathematical tools are reviewed and key derivations are presented in the Appendices.

2 Gain and Effective Area

Antenna gain describes how an antenna converts input power into radiation in a specified direction $\hat{\boldsymbol{r}}$, [4]. The gain in a direction $\hat{\boldsymbol{r}}$ is determined as 4π times the quotient between the radiation intensity $P(\hat{\boldsymbol{r}})$ and the dissipated power $P_\mathrm{r} + P_\Omega$,

$$G(\hat{\boldsymbol{r}}) = 4\pi \frac{P(\hat{\boldsymbol{r}})}{P_\mathrm{r} + P_\Omega}, \tag{2.1}$$

where P_r and P_Ω denote the radiated power and power dissipated in ohmic and dielectric losses, respectively. The effective area, A_eff, is an alternative quantity used to describe directive properties for receiving antennas, which is for reciprocal antennas simply related to the gain as [53]

$$A_\mathrm{eff} = \frac{G\lambda^2}{4\pi}, \tag{2.2}$$

where $\lambda = 2\pi/k$ denotes the wavelength. It is seen that maximization of gain is equivalent to maximization of effective area [27].

The optimized parameters are expressed in the current density $\boldsymbol{J}(\boldsymbol{r})$ which is expanded in a set of basis functions $\{\boldsymbol{\psi}_n(\boldsymbol{r})\}$ as [27]

$$\boldsymbol{J}(\boldsymbol{r}) \approx \sum_{n=1}^{N} I_n \boldsymbol{\psi}_n(\boldsymbol{r}), \tag{2.3}$$

where the expansion coefficients, I_n, are collected in the column matrix $\mathbf{I}$. This substitution yields algebraic expressions for radiation intensity, radiated power, and

ohmic losses as follows [17]

$$P(\hat{\boldsymbol{r}}) \approx \frac{1}{2}\left|\mathbf{F}\mathbf{I}\right|^2 = \frac{1}{2}\mathbf{I}^{\mathrm{H}}\mathbf{F}^{\mathrm{H}}\mathbf{F}\mathbf{I}, \tag{2.4}$$

$$P_{\mathrm{r}} \approx \frac{1}{2}\mathbf{I}^{\mathrm{H}}\mathbf{R}_{\mathrm{r}}\mathbf{I}, \tag{2.5}$$

$$P_{\Omega} \approx \frac{1}{2}\mathbf{I}^{\mathrm{H}}\mathbf{R}_{\Omega}\mathbf{I}. \tag{2.6}$$

The matrices used in (2.4)–(2.6) are reviewed in Appendix A. Substitution of (2.4)–(2.6) into (2.1) yields

$$G(\hat{\boldsymbol{r}}) \approx 4\pi\frac{\left|\mathbf{F}\mathbf{I}\right|^2}{\mathbf{I}^{\mathrm{H}}(\mathbf{R}_{\mathrm{r}}+\mathbf{R}_{\Omega})\mathbf{I}} = 4\pi\frac{\mathbf{I}^{\mathrm{H}}\mathbf{U}\mathbf{I}}{\mathbf{I}^{\mathrm{H}}(\mathbf{R}_{\mathrm{r}}+\mathbf{R}_{\Omega})\mathbf{I}}, \tag{2.7}$$

where we also introduced the matrix $\mathbf{U} = \mathbf{F}^{\mathrm{H}}\mathbf{F}$ to simplify the notation and highlight the expression of the gain $G(\hat{\boldsymbol{r}})$ as a Rayleigh quotient.

2.1 Maximum Gain: Tuned Case

The maximum gain for antennas confined to a region $\boldsymbol{r} \in \Omega$ is formulated as the optimization problem

$$\begin{aligned} &\text{maximize} && \mathbf{I}^{\mathrm{H}}\mathbf{U}\mathbf{I} \\ &\text{subject to} && \mathbf{I}^{\mathrm{H}}(\mathbf{R}_{\Omega}+\mathbf{R}_{\mathrm{r}})\mathbf{I} = 1, \end{aligned} \tag{2.8}$$

where for simplicity the dissipated power is normalized to unity. This problem is equivalent to the Rayleigh quotient

$$G_{\mathrm{ub}} \approx 4\pi \max_{\mathbf{I}} \frac{\mathbf{I}^{\mathrm{H}}\mathbf{F}^{\mathrm{H}}\mathbf{F}\mathbf{I}}{\mathbf{I}^{\mathrm{H}}(\mathbf{R}_{\mathrm{r}}+\mathbf{R}_{\Omega})\mathbf{I}}, \tag{2.9}$$

to which a solution is found via the generalized eigenvalue problem [27]

$$\mathbf{F}^{\mathrm{H}}\mathbf{F}\mathbf{I} = \gamma(\mathbf{R}_{\mathrm{r}}+\mathbf{R}_{\Omega})\mathbf{I}. \tag{2.10}$$

In order to reduce the computational burden, the formula (2.10) is further transformed to

$$(\mathbf{R}_{\mathrm{r}}+\mathbf{R}_{\Omega})^{-1}\,\mathbf{F}^{\mathrm{H}}\mathbf{F}\mathbf{I} = \gamma\mathbf{I} \tag{2.11}$$

and multiplied from left by the matrix $\mathbf{F}$. By introducing $\tilde{\mathbf{I}} = \mathbf{F}\mathbf{I}$ we readily get

$$\mathbf{F}(\mathbf{R}_{\mathrm{r}}+\mathbf{R}_{\Omega})^{-1}\mathbf{F}^{\mathrm{H}}\tilde{\mathbf{I}} = \gamma\tilde{\mathbf{I}}. \tag{2.12}$$

Taking into account that the far-field matrix $\mathbf{F}$ can be expressed using two orthogonal polarizations, see Appendix A, the original $N \times N$ eigenvalue problem (2.10) is reduced into the 2×2 eigenvalue problem (2.12) which can be written as

$$G_{\mathrm{ub}} \approx 4\pi \max \mathrm{eig}(\mathbf{F}(\mathbf{R}_{\mathrm{r}}+\mathbf{R}_{\Omega})^{-1}\mathbf{F}^{\mathrm{H}}) \tag{2.13}$$

with the optimal current determined as

$$\mathbf{I} = \gamma^{-1}(\mathbf{R}_\mathrm{r} + \mathbf{R}_\Omega)^{-1}\mathbf{F}^\mathrm{H}\tilde{\mathbf{I}}. \tag{2.14}$$

The corresponding case with the partial gain contains one polarization direction and hence the eigenvalue $\gamma = \mathbf{F}(\mathbf{R}_\mathrm{r} + \mathbf{R}_\Omega)^{-1}\mathbf{F}^\mathrm{H}$ and current

$$\mathbf{I} \sim (\mathbf{R}_\mathrm{r} + \mathbf{R}_\Omega)^{-1}\mathbf{F}^\mathrm{H}. \tag{2.15}$$

Here, the $\mathbf{F}^\mathrm{H}$ part can be interpreted as phase conjugation of an incident plane wave from the $\hat{\boldsymbol{r}}$-direction, and hence the current corresponding to the maximum gain is found by phase conjugation of the incident wave modified by $(\mathbf{R}_\mathrm{r} + \mathbf{R}_\Omega)^{-1}$.

2.2 Maximum Gain: Self-Resonant Case

The solution to (2.13) is in general not self-resonant. Self resonance is enforced to (2.13) by adding the constraint of zero reactance, $\mathbf{I}^\mathrm{H}\mathbf{X}\mathbf{I} = 0$, see Appendix A, producing the optimization problem

$$\begin{aligned} \text{maximize} \quad & \mathbf{I}^\mathrm{H}\mathbf{U}\mathbf{I} \\ \text{subject to} \quad & \mathbf{I}^\mathrm{H}\mathbf{X}\mathbf{I} = 0 \\ & \mathbf{I}^\mathrm{H}(\mathbf{R}_\Omega + \mathbf{R}_\mathrm{r})\mathbf{I} = 1. \end{aligned} \tag{2.16}$$

This optimization problem is a quadratically constrained quadratic program (QCQP), see Appendix B, that is transformed to a dual problem by multiplication of $\mathbf{I}^\mathrm{H}\mathbf{X}\mathbf{I}$ with a scalar parameter ν and adding the constraints together, *i.e.*,

$$\begin{aligned} \text{maximize} \quad & \mathbf{I}^\mathrm{H}\mathbf{U}\mathbf{I} \\ \text{subject to} \quad & \mathbf{I}^\mathrm{H}(\nu\mathbf{X} + \mathbf{R}_\Omega + \mathbf{R}_\mathrm{r})\mathbf{I} = 1, \end{aligned} \tag{2.17}$$

which is solved as a generalized eigenvalue problem analogously to Section 2.1. The solution to this problem is greater or equal to (2.16) and taking its minimum value produces the dual problem [8]

$$\begin{aligned} G_\mathrm{ub,r} &\approx 4\pi \min_\nu \max \mathrm{eig}(\mathbf{U}, \nu\mathbf{X} + \mathbf{R}_\Omega + \mathbf{R}_\mathrm{r}) \\ &= 4\pi \min_\nu \max \mathrm{eig}(\mathbf{F}(\nu\mathbf{X} + \mathbf{R}_\Omega + \mathbf{R}_\mathrm{r})^{-1}\mathbf{F}^\mathrm{H}) \end{aligned} \tag{2.18}$$

which is convex and easy to solve, *e.g.*, with the bisection algorithm [43]. The derivative of the eigenvalue γ with respect to ν is [38]

$$\frac{\partial\gamma}{\partial\nu} = -\gamma^2\frac{\mathbf{I}^\mathrm{H}\mathbf{X}\mathbf{I}}{\mathbf{I}^\mathrm{H}\mathbf{U}\mathbf{I}} \begin{cases} \leq 0 & \text{for } \nu \leq \nu_\mathrm{opt}, \quad \text{inductive} \\ = 0 & \text{for } \nu = \nu_\mathrm{opt}, \quad \text{resonant} \\ \geq 0 & \text{for } \nu \geq \nu_\mathrm{opt}, \quad \text{capacitive} \end{cases} \tag{2.19}$$

for cases with non-degenerate eigenvalues. Degenerate eigenvalues are often related to geometrical symmetries and solved by decomposition of the current $\mathbf{I}$ into orthogonal sub-spaces [9]. The range $\nu \in [\nu_\mathrm{min}, \nu_\mathrm{max}]$ in (2.18) is determined from the

condition $\nu\mathbf{X}+\mathbf{R}_\Omega+\mathbf{R}_\mathrm{r}\succeq\mathbf{0}$ which can be computed from the smallest and largest eigenvalues, $\mathrm{eig}(\mathbf{X},\mathbf{R}_\Omega+\mathbf{R}_\mathrm{r})$, *i.e.*,

$$\frac{-1}{\max\mathrm{eig}(\mathbf{X},\mathbf{R}_\Omega+\mathbf{R}_\mathrm{r})}\leq\nu\leq\frac{-1}{\min\mathrm{eig}(\mathbf{X},\mathbf{R}_\Omega+\mathbf{R}_\mathrm{r})}, \tag{2.20}$$

see Appendix E for details.

The minimal eigenvalue $\min\mathrm{eig}(\mathbf{X},\mathbf{R}_\Omega+\mathbf{R}_\mathrm{r})$ is related to the Q-factor of the maximal capacitance in the geometry which is very large for all considered cases giving an upper limit very close to zero and $\nu_\mathrm{max}\to 0$ as the mesh is refined. The maximal eigenvalue is related to the maximal inductive Q-factor which is a fixed value depending on shape of the object and gives the lower bound ν_min, *cf.* with the inductor Q-factor in [15].

2.3 Examples of Maximum Gain and Effective Area

The following section presents maximum gain and effective area for examples of various complexity:

1. spherical shell both for externally and self-resonant currents, Section 2.3.1,
2. comparison of end-fire and broadside radiation from a rectangular region, Section 2.3.2,
3. maximization of effective area if different parts of a cylinder are considered, Section 2.3.3,
4. limited controllability of currents for a parabolic dish with spherical prime feed, Section 2.3.4.

2.3.1 Externally tuned and self-resonant currents (spherical shell)

Expansion of the current density on a spherical shell in vector spherical harmonics [37] produces diagonal reactance $\mathbf{X}$, radiation resistance $\mathbf{R}_\mathrm{r}$, and loss $\mathbf{R}_\Omega$ matrices with closed form expressions of the elements. The direction of radiation can without loss of generality be chosen to $\hat{\boldsymbol{r}}=\hat{\boldsymbol{z}}$ for which the elements $\mathbf{F}$ are zero for azimuthal Fourier indices $|m|\neq 1$. It is hence sufficient to consider $|m|=1$ for the radiation, see Appendix F.

The maximum gain for a spherical shell with surface resistivity $R_\mathrm{s}=10^{-n}\,\Omega/\square$ for $n=\{0,2,4,6,8\}$ is determined using (2.13), (2.18) and depicted in Fig. 1. The results are compared with the estimates $G_\mathrm{H}=(ka)^2+2ka$ by Harrington [25] and from the geometrical cross section $G_\mathrm{GO}=4\pi A_\mathrm{cross}/\lambda^2$. It is observed that the additional constraint on self-resonance, *i.e.*, $\mathbf{I}^\mathrm{H}\mathbf{X}\mathbf{I}=0$, in (2.16) has a large effect for small structures ($ka<1$) but negligible effect for electrically large structures. The tuned and self-resonant cases have $D=3/2$ and $D=3$, respectively, in the limit of electrically small structures ($ka\to 0$), see Appendix F. Onset of spherical modes for small ka gives a step-wise increasing directivity and gain, see figures in Appendix F. Dependence on R_s diminishes and the gain approaches G_GO as ka increases.

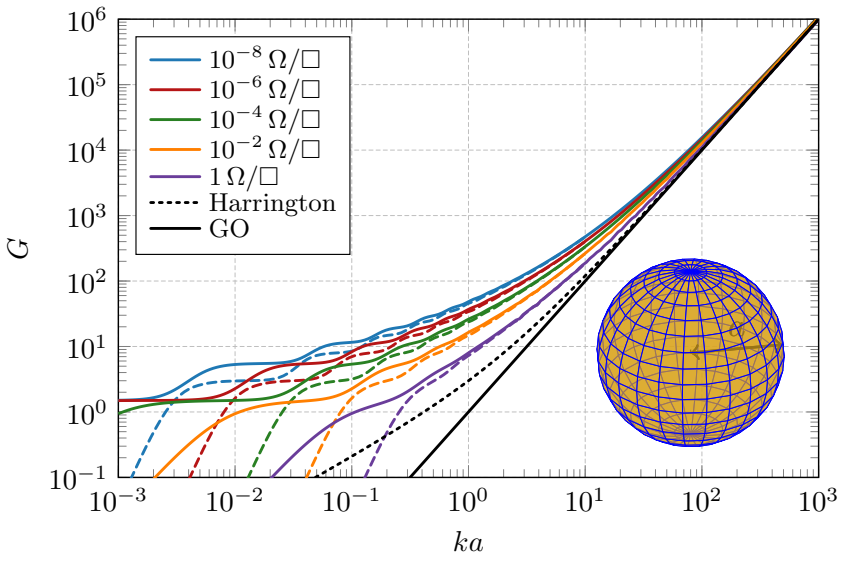

Figure 1: Maximum gain for a spherical shell of radius a with surface resistivity $R_\mathrm{s} = 10^{-n}\,\Omega/\square$, $n = \{0, 2, 4, 6, 8\}$, both for externally tuned (2.13), G_ub, (solid lines) and for self-resonant (2.18), $G_\mathrm{ub,r}$, (dashed lines) currents.

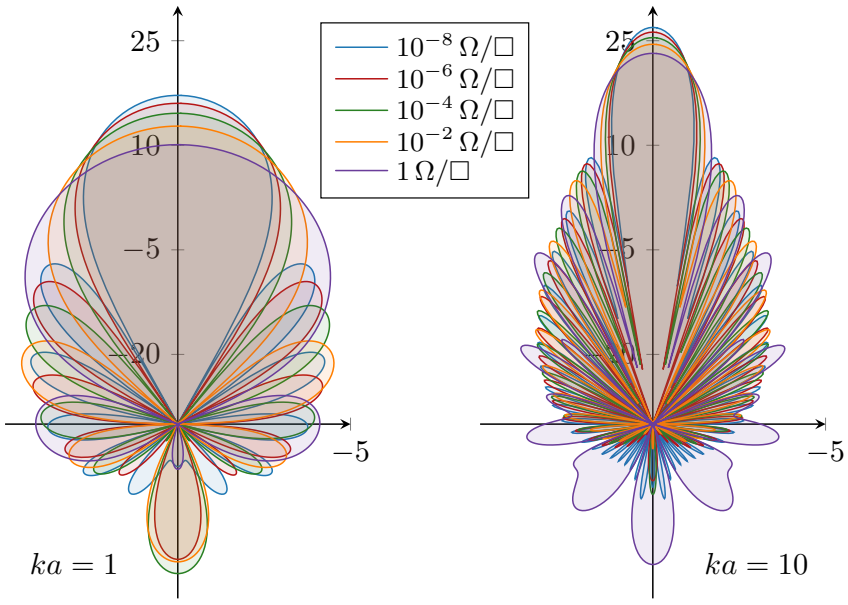

Figure 2: Radiation patterns for a spherical shell of radius a with surface resistivity $R_\mathrm{s} = 10^{-n}\,\Omega/\square$, $n = \{0, 2, 4, 6, 8\}$ corresponding to the externally tuned case in Fig. 1. The radiation patterns are shown in terms of gain G for a ϑ-cut and $\varphi = 0$. The two electrical sizes, $ka = 1$ and $ka = 10$, are depicted.

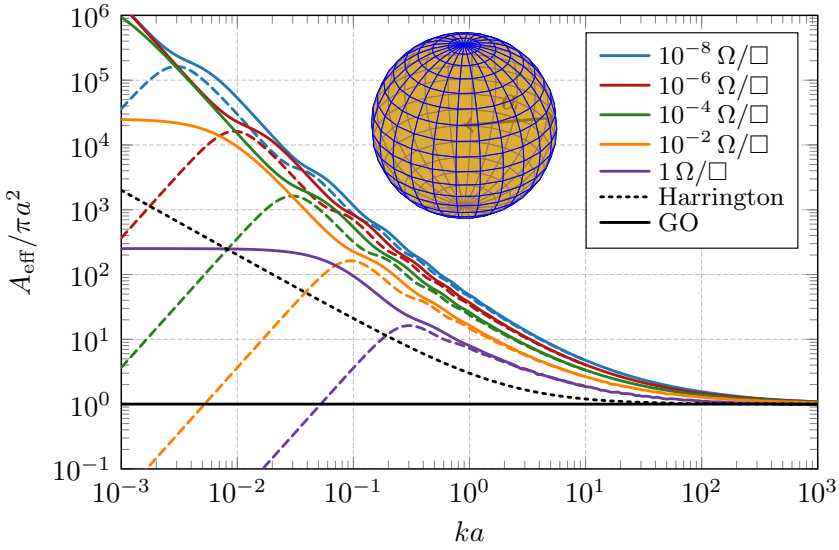

Figure 3: Maximum effective area for a spherical shell of radius a with surface resistivity $R_{\text{s}} = 10^{-n}\,\Omega/\square$, $n = \{0, 2, 4, 6, 8\}$, both for externally tuned (2.13) (solid lines) and for self-resonant (2.18) (dashed lines) currents.

The radiation patterns and the influence of the surface resistivity on the maximum gain G is shown in Fig. 2 for the externally tuned case and electrical sizes $ka = 1$ and $ka = 10$. The electrically large limit is more clearly seen by plotting the effective area (2.2) in Fig. 3, where it is observed that the effective area approaches the cross-section area as $ka \to \infty$.

2.3.2 Broadside and end-fire radiation (rectangular plate)

The symmetry of the sphere is ideal for analytic solution of the optimization problem but cannot be used to investigate important cases such as broadside and end-fire radiation [13]. Let us, therefore, consider a planar rectangular plate with side lengths ℓ and $\ell/2$ placed at $z = 0$ having surface resistivity $R_{\text{s}} = 10^{-4} Z_0$ per square. The maximum effective area is depicted in Fig. 4 for radiation in the cardinal directions. Three regions can be identified: electrically small ($ka \ll 1$) with large difference between the externally tuned and self-resonant cases, intermediate region with dominant end-fire radiation, and electrically large $ka \gg 1$ with dominant broadside radiation.

Negligible directional differences are observed for the electrically small ($ka \ll 1$) externally tuned case which can be explained by radiation patterns originating from electric dipoles. The effective area for the self-resonant case deceases as $(ka)^2$ and consists of a combination of electric and magnetic dipoles. Huygens sources are obtained for the end-fire cases where the gain is higher for radiation along the longest side than for the shorter side due to its lower amount of stored electric energy. Gain in the broadside direction is lower due to its up-down symmetric radiation pattern.

The difference between the externally tuned and self-resonant cases decreases as

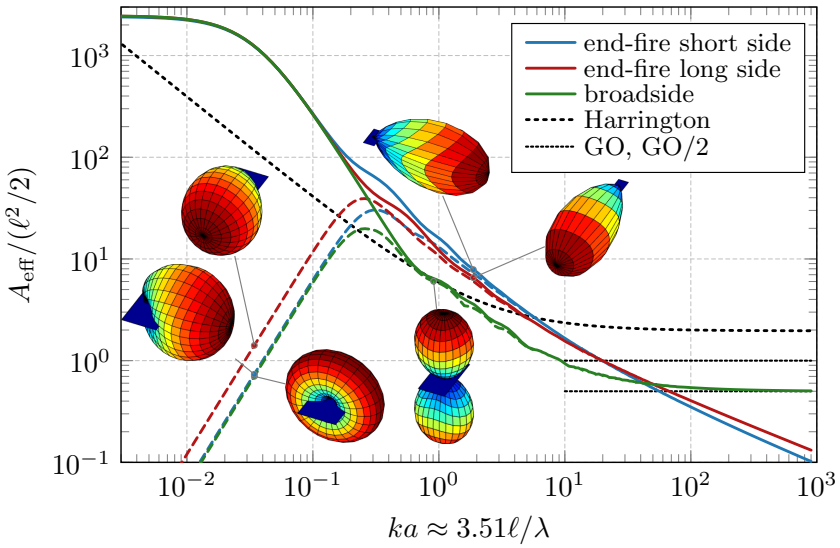

Figure 4: Maximum effective area in the cardinal directions for a rectangular plate with size $\ell \times \ell/2$ and surface resistivity $R_{\text{s}} = 10^{-4}Z_0$ per square. Bounds for externally tuned (2.13) (solid lines) and self-resonant (2.16) (dashed lines) currents are depicted.

ka increases and become negligible around $ka \approx 1$. Here, it is also seen that the effective area for the self-resonant case has a maximum around the same size. The end-fire directions have higher effective area (and gain) than the broadside direction up to $ka \approx 50$. Approaching the electrically large region ($ka \to \infty$), the broadside radiation converges to one half of the physical cross section area since the electric currents produce symmetric radiation patterns in up-down direction, and the end-fire directions are observed to decay approximately as $(ka)^{-1/2}$.

2.3.3 Contribution to the maximum effective area (cylinder)

The maximum effective area is studied in this example for a single disc Ω_{t}, two separated discs $\Omega_{\text{t}} \cup \Omega_{\text{b}}$, a mantel surface Ω_{m} and a cylinder $\Omega_{\text{t}} \cup \Omega_{\text{b}} \cup \Omega_{\text{m}}$.

The performance of a single disc Ω_{t} with radius r depicted in Fig. 5 confirms the broadside limit $A_{\text{eff}} \to A_{\text{cross}}/2$ in the electrically large region as observed for the rectangle in Fig. 4. The stepwise decrease for smaller sizes can be interpreted as the onset of spherical modes in agreement with the sphere in Fig. 1. Addition of a second disc separated by the distance $2r$ from the first disc breaks the up-down symmetry of the radiation pattern. The effective area is depicted in Fig. 5 with the curve labeled $\Omega_{\text{t}} \cup \Omega_{\text{b}}$. A rapid oscillatory behavior is observed for electrically large structures. These oscillations are due to the up-down symmetry for disc distances of integer multiples of the wavelength, *i.e.*, the radiation in the $\pm\hat{\boldsymbol{z}}$-directions are identical, where $\hat{\boldsymbol{z}}$ denotes the axis of rotation. For other distances the radiation from the discs can contribute constructively in the $\hat{\boldsymbol{z}}$-direction and destructively in the $-\hat{\boldsymbol{z}}$-direction. This produces an effective area approaching A_{cross} on average in the electrically large ($ka \to \infty$) region.

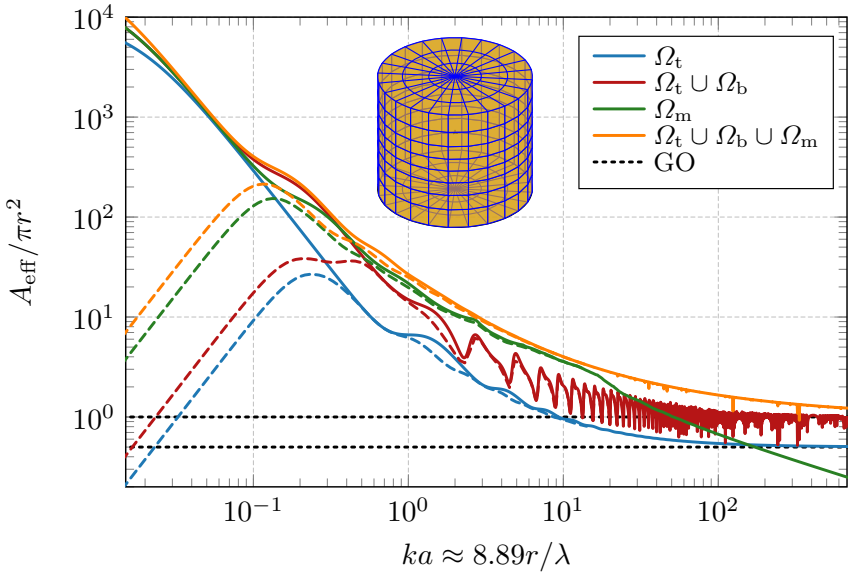

Figure 5: Maximum effective area for a disc, two discs, a mantel surface, and a cylindrical structure with surface resistivity $R_{\text{s}} = 10^{-2}\,\Omega/\square$ in the axial ($\hat{\boldsymbol{z}}$)-direction. Bounds for externally tuned (2.13) (solid lines) and self-resonant (2.16) (dashed lines) currents are depicted.

End-fire radiation is considered from the mantel surface Ω_{m} (the hollow cylindrical structure without top and bottom discs) in Fig. 5. The effective area decreases approximately linearly in the log-log scale giving the approximate scaling $A_{\text{eff}} \sim (ka)^{-1/2}$ as also seen in Fig. 4. Here, it is also observed that the effect of resistivity is larger for the end-fire case as compared to the broadside cases.

Adding the bottom and top discs to the cylinder mantel surface forms a cylindrical shell as shown in Fig. 5. The effective area approaches A_{cross} similar to the discs case but with most of the oscillations removed.

2.3.4 Controllable currents (parabolic reflector)

A parabolic reflector is used to illustrate the effective area for controllable substructures, see Fig. 6. The parabolic reflector is rotationally symmetric and has radius a, focal distance $a/2$, and depth $a/2$. A sphere with radius $r = a/20$ is placed in the focal point. Maximum effective area is depicted for three cases: controllable currents on the parabolic reflector and sphere, controllable currents on the reflector, and controllable currents on the sphere. The induced currents are determined from the method of moments (MoM) impedance matrix [16]. Controlling both the reflector and sphere gives the largest effective area and approaches the cross section area for electrically large structures as seen in Fig. 6. The oscillations starting around $ka \approx 55$ originates in the internal resonances of the sphere, where it is noted that $kr \approx 2.74$ in agreement with the TE dipole resonance [26]. This is also confirmed by negligible impact on the overall behavior of the effective area from using smaller and larger spheres except for shifting of the resonances up and

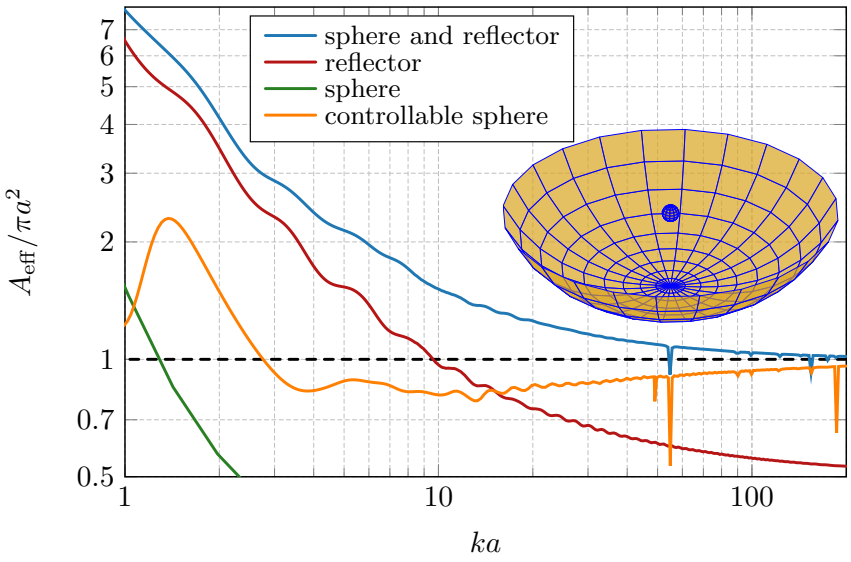

Figure 6: Maximum effective area from (2.13) for a parabolic reflector combined with a sphere placed in the focal point with surface resistivity $R_{\text{s}} = 10^{-2}\,\Omega/\square$ in the axial ($\hat{\boldsymbol{z}}$)-direction. The parabolic reflector has radius a, focal distance $a/2$, and depth $a/2$ and the sphere has radius $r = a/20$.

down. However, the scenario with both reflector and the prime feeder controllable is unrealistic.

Removing the sphere and optimizing the currents on the reflector lowers the effective area with approximately a factor of two for large ka. This might at first seem surprising as the cross-section area of the reflector is 400 times larger than for the sphere having radius $r = a/20$. Moreover, the effective area of the sphere is close to its cross-section area, *i.e.*, $A_{\text{eff}} \approx \pi r^2 \approx A_{\text{cross}}/400$ as seen in Fig. 3. The effective area of the reflector is better explained by its similarity to the disc in Fig. 5 and rectangle in Fig. 4, where the asymptotic limit $A_{\text{cross}}/2$ is explained by the up-down symmetry of the radiation pattern. The limit $A_{\text{eff}} \approx A_{\text{cross}}$ for the reflector together with the sphere is hence explained by elimination of the backward radiation.

Replacing the controllable currents on the reflector with induced currents from the sphere produces an effective area just below A_{cross} for high ka. The reduction for small ka is similar to the short circuit of the currents above a ground plane. Internal resonances for the sphere are more emphasized as all radiation originates from the sphere in this case.

3 Superdirectivity

Directional properties of the radiation pattern are quantified by the directivity

$$D(\hat{\boldsymbol{r}}) = 4\pi \frac{P(\hat{\boldsymbol{r}})}{P_{\text{r}}} \approx 4\pi \frac{\mathbf{I}^{\text{H}}\mathbf{U}\mathbf{I}}{\mathbf{I}^{\text{H}}\mathbf{R}_{\text{r}}\mathbf{I}}. \tag{3.1}$$

Here, it is seen that the directivity (3.1) only differs from the gain (2.1) by its normalization with the radiated power instead of the total dissipated power. This difference is the radiation efficiency $\eta = P_\mathrm{r}/(P_\mathrm{r} + P_\Omega)$, which is related to the dissipation factor

$$\delta = \frac{P_\Omega}{P_\mathrm{r}} \approx \frac{\mathbf{I}^\mathrm{H}\mathbf{R}_\Omega\mathbf{I}}{\mathbf{I}^\mathrm{H}\mathbf{R}_\mathrm{r}\mathbf{I}}. \tag{3.2}$$

Directivity higher than a nominal directivity is often referred to as superdirectivity and associated with low efficiency and narrow bandwidth [21]. The trade-off between the Q-factor and directivity was shown in [16] and further investigated in [17, 19, 32]. Superdirectivity is also associated with decreased radiation efficiency or equivalently an increased dissipation factor (3.2).

3.1 Trade-off Between Dissipation Factor and Directivity

The trade-off between losses and directivity for a self-resonant antenna can be analyzed by separating the radiated power P_r and losses P_Ω in (2.16) giving the optimization problem

$$\begin{aligned} \text{maximize} \quad & \mathbf{I}^\mathrm{H}\mathbf{U}\mathbf{I} \\ \text{subject to} \quad & \mathbf{I}^\mathrm{H}\mathbf{X}\mathbf{I} = 0 \\ & \mathbf{I}^\mathrm{H}\mathbf{R}_\mathrm{r}\mathbf{I} = 1 \\ & \mathbf{I}^\mathrm{H}\mathbf{R}_\Omega\mathbf{I} = \delta. \end{aligned} \tag{3.3}$$

The constraint $\mathbf{I}^\mathrm{H}\mathbf{X}\mathbf{I} = 0$ is dropped for the corresponding non-self resonant case (2.7). The Pareto front is formed by adding the constraints weighted by scalar parameters, *i.e.*,

$$\begin{aligned} \text{maximize} \quad & \mathbf{I}^\mathrm{H}\mathbf{U}\mathbf{I} \\ \text{subject to} \quad & \mathbf{I}^\mathrm{H}(\nu\mathbf{X} + \alpha\mathbf{R}_\Omega + \mathbf{R}_\mathrm{r})\mathbf{I} = 1, \end{aligned} \tag{3.4}$$

where the right-hand side is re-normalized to unity without restriction of generality. This problem is identical to the maximum gain problem (2.17) if the Pareto parameter $\alpha \geq 0$ is included in the surface resistivity R_s and is hence solved as the eigenvalue problem (2.18). Here, $\alpha = 0$ solely weights the radiated power regardless of ohmic losses and increasing α starts to emphasize ohmic losses. The maximal directivity ($\alpha = 0$) is in general unbounded [7, 44] but has low gain. The other extreme point $\alpha \to \infty$ neglects the radiated power and maximizes D/δ, *i.e.*, the quotient between the directivity and dissipation factor.

The minimum dissipation factor for the rectangular plate from Fig. 4 as a function of the directivity in the cardinal directions and its corresponding case with maximum gain as a function of surface resistivity R_s are shown in Fig. 7 and Fig. 8, respectively. Although the physical interpretation of these two problems is different, they are both solved using the same eigenvalue problem and have identical current densities, *i.e.*, the optimal currents were found using (2.12) which is identical to (3.4) without the $\mathbf{X}$-term. Consider, *e.g.*, the blue curve depicting end-fire radiation along the short side. The normalized dissipation factor is monotonically increasing with D

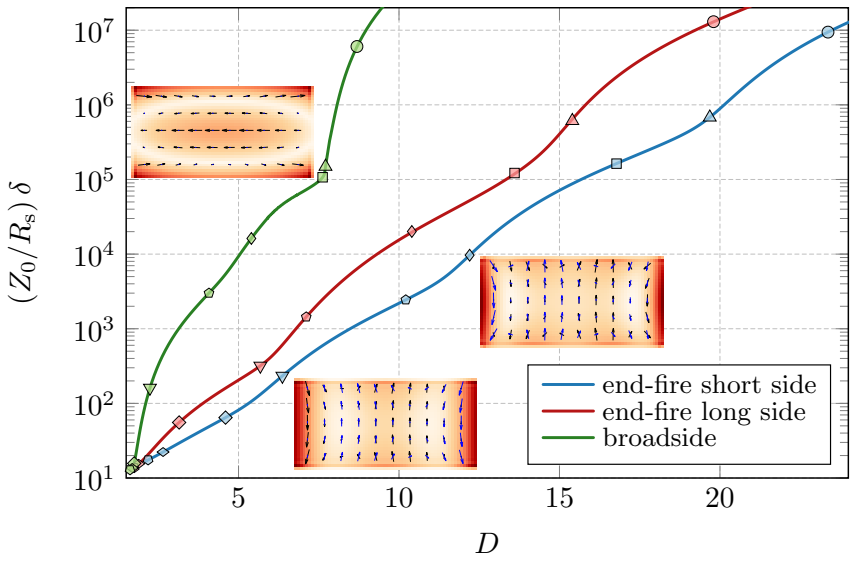

Figure 7: Minimum externally tuned dissipation factor for a rectangular plate of side aspect ratio 2 : 1 and electrical size $ka = 1$ as a function of directivity D in the cardinal directions. The corresponding case with maximum gain is depicted in Fig. 8.

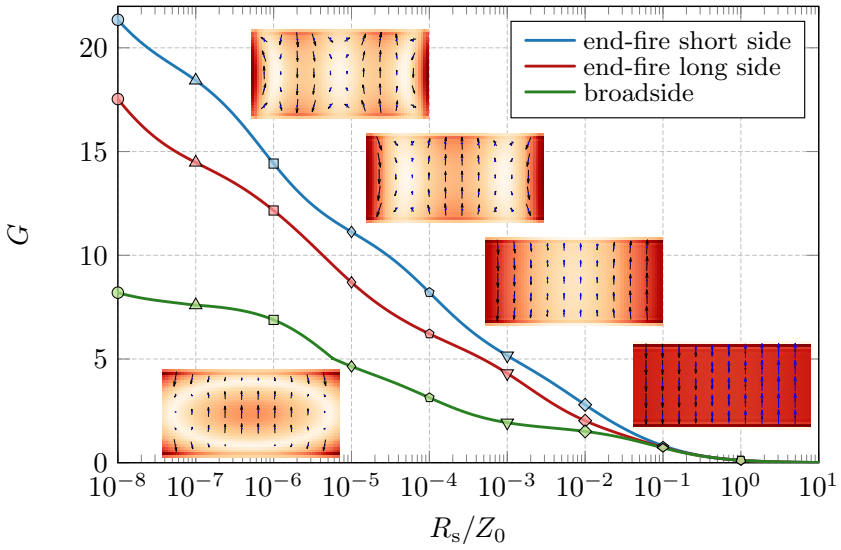

Figure 8: Maximum externally tuned gain for a rectangular plate of side aspect ratio 2 : 1 and electrical size $ka = 1$ as a function of surface resistivity R_s. The current density is depicted for $R_\mathrm{s} \in \{10^{-6}, 10^{-4}, 10^{-2}, 1\}Z_0$ and $R_\mathrm{s} = 10^{-5}Z_0$ for radiation in end-fire short side and broadside directions, respectively, see also Fig. 7.

from approximately 10 for $D \approx 2$ to 10^7 for $D \approx 25$ showing that an increased directivity comes with a high cost in losses. The corresponding blue curve in Fig. 8 decreases monotonically with the surface resistivity R_s from $G \approx 22$ for $R_\mathrm{s} = 10^{-8} Z_0$ to $G \approx 0.1$ for $R_\mathrm{s} = Z_0$. The current density is depicted for $R_\mathrm{s} \in \{10^{-6}, 10^{-4}, 10^{-2}\} Z_0$ in Fig. 8 and $R_\mathrm{s} \in \{10^{-5}, 10^{-3}\} Z_0$ in Fig. 7, where it is seen that the oscillations in the current density increase for high D and low R_s. Moreover, the markers on each curve in Fig. 7 and Fig. 8 correspond to points with identical current densities. Here, it is seen that the uniform spacing in Fig. 8 is not preserved in Fig. 7, *e.g.*, the green curve depicting broadside radiation has two almost overlapping points around $D \approx 8$ and $(Z_0/R_\mathrm{s})\delta \approx 10^5$. These two points also have close to orthogonal current densities as seen by the insets and correspond to cases where the eigenvalue problem (3.4) has degenerate eigenvalues. For these cases we use linear combinations between the eigenvectors to span the Pareto curve [9].

The minimum dissipation factor [15, 30, 56] is lower than the dissipation factor obtained from the $\alpha \to \infty$ case for electrically large structures. These limit cases are connected by reformulating the problem (3.3) by either minimizing the ohmic losses or maximizing the radiated power. Minimization of ohmic losses subject to fixed radiation intensity and radiated power is

$$\begin{aligned} \text{minimize} \quad & \mathbf{I}^\mathrm{H} \mathbf{R}_\Omega \mathbf{I} \\ \text{subject to} \quad & \mathbf{I}^\mathrm{H} \mathbf{X} \mathbf{I} = 0 \\ & \mathbf{I}^\mathrm{H} \mathbf{U} \mathbf{I} = 2P \\ & \mathbf{I}^\mathrm{H} \mathbf{R}_\mathrm{r} \mathbf{I} = 2P_\mathrm{r}, \end{aligned} \tag{3.5}$$

which is relaxed to

$$\begin{aligned} \text{minimize} \quad & \mathbf{I}^\mathrm{H} \mathbf{R}_\Omega \mathbf{I} \\ \text{subject to} \quad & \mathbf{I}^\mathrm{H} (\nu \mathbf{X} + \alpha \mathbf{U} + \mathbf{R}_\mathrm{r}) \mathbf{I} = 1, \end{aligned} \tag{3.6}$$

where again the right-hand side is re-normalized to unity.

3.2 Trade-off Between Q-factor and Directivity

Superdirectivity is also associated with narrow bandwidth and high Q-factor [16, 32]. Adding constraints on the stored energy to the optimization problem (3.3) results in the optimization problem

$$\begin{aligned} \text{maximize} \quad & \mathbf{I}^\mathrm{H} \mathbf{U} \mathbf{I} \\ \text{subject to} \quad & \mathbf{I}^\mathrm{H} \mathbf{X} \mathbf{I} = 0 \\ & \mathbf{I}^\mathrm{H} (\mathbf{X}_\mathrm{e} + \mathbf{X}_\mathrm{m}) \mathbf{I} = 2Q \\ & \mathbf{I}^\mathrm{H} \mathbf{R}_\Omega \mathbf{I} = \delta \\ & \mathbf{I}^\mathrm{H} \mathbf{R}_\mathrm{r} \mathbf{I} = 1, \end{aligned} \tag{3.7}$$

where $\mathbf{X}_\mathrm{e} + \mathbf{X}_\mathrm{m} = k \partial \mathbf{X} / \partial k$ are matrices used to determine the stored energy [17, 58]. Forming linear combinations between the constraints is used to determine the Pareto front and analyzing the trade-off between directivity, Q-factor, and dissipation factor.

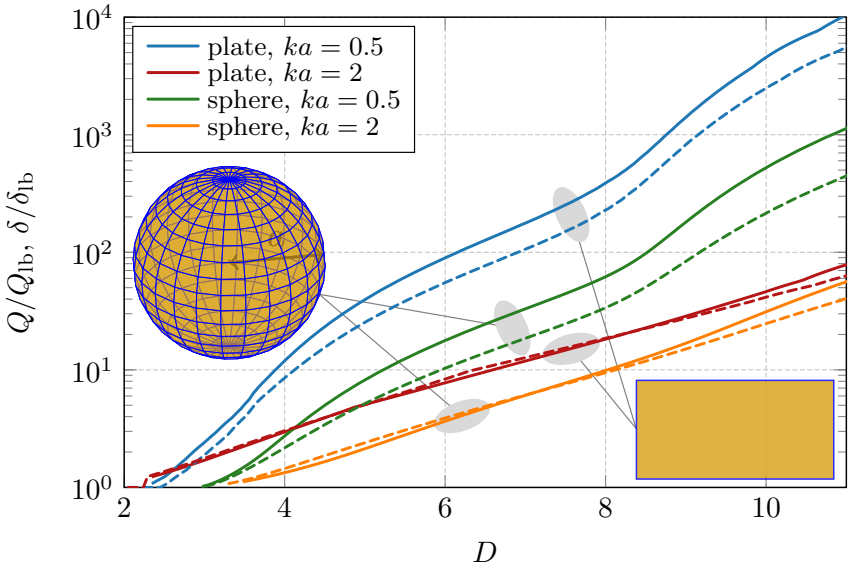

Figure 9: Lower bounds on dissipation (solid lines) and Q-factors (dashed lines) for prescribed directivity D normalized with respect the lower bounds. The results were calculated for a spherical shell of radius a and a rectangular plate of side aspect ratio $2:1$. The electrical size used is $ka \in \{0.5, 2\}$ and the currents are self-resonant.

Although (3.7) can be used to analyze the trade-off, it is illustrative to focus on the constraints on the dissipation factor and Q-factor separately. Dropping the constraint on the ohmic losses reduces (3.7) to the problem of lower bounds on the Q-factor for a given directivity [16] which is relaxed to

$$\begin{aligned} &\text{maximize} && \mathbf{I}^{\mathrm{H}}\mathbf{U}\mathbf{I} \\ &\text{subject to} && \mathbf{I}^{\mathrm{H}}(\nu\mathbf{X} + \alpha(\mathbf{X}_{\mathrm{e}} + \mathbf{X}_{\mathrm{m}}) + \mathbf{R}_{\mathrm{r}})\mathbf{I} = 1, \end{aligned} \tag{3.8}$$

and solved analogously to (2.18) for fixed α. Here, $\alpha = 0$ solely weights the radiated power regardless of ohmic losses and increasing α starts to emphasize ohmic losses. The maximal directivity ($\alpha = 0$) is in general unbounded [7, 44] but has a high Q-factor. Here, reformulations similar to (3.5) can be used to reach the lower bound on the Q-factor.

The trade-offs between directivity and dissipation factor and Q-factor are compared in Fig. 9 for a spherical shells and a rectangular plate of size $ka \in \{0.5, 2\}$. The bounds are normalized with the lower bounds on the dissipation and Q-factors for the structure. The stored energy matrices are transformed to be positive semi-definite for the Q-factor calculation [16].

4 Radiation Modes and Degrees of Freedom

The maximum gain was expressed by Harrington in spherical mode expansion as [25]

$$G_{\mathrm{H}} = L^2 + 2L = \frac{N_{\mathrm{DoF}}}{2}, \tag{4.1}$$

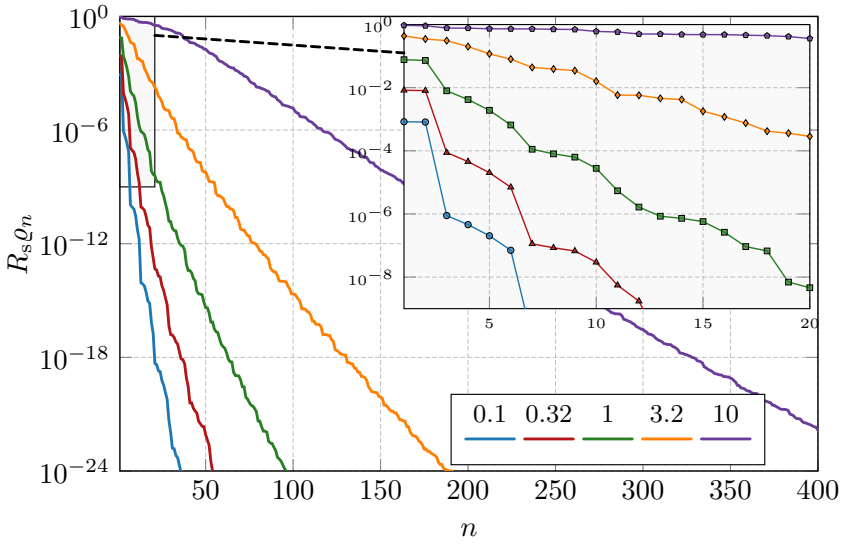

Figure 10: Radiation modes for a rectangular plate of side aspect ratio 2 : 1 and electrical sizes $ka \in \{0.1, 0.32, 1, 3.2, 10\}$.

where L is the order of the spherical modes and N_{DoF} degrees of freedom, *i.e.*, total number of modes [35]. The maximum gain is related to the size of an antenna aperture ka by a cut off limit for modes $L = ka$ [26], but should be corrected for $ka < 1$ as $L \geq 1$, see also [35]. This spherical mode expansion is most suitable for spherical geometries but overestimates the number of modes for other shapes.

In order to take a specific shape of an antenna into account, the modes maximizing the radiated power P_{r} over the lost power P_Ω, *i.e.*, those minimizing dissipation factor δ, are found from an eigenvalue problem [15, 25, 30] as

$$\mathbf{R}_{\text{r}}\mathbf{I}_n = \varrho_n R_{\text{s}} \mathbf{\Psi} \mathbf{I}_n, \tag{4.2}$$

where $\mathbf{R}_\Omega = R_{\text{s}}\mathbf{\Psi}$ was substituted on the right-hand side, and only modes with $\delta_n = \varrho_n^{-1} < 1$ are considered here as well-radiating. It can be seen in (4.2) that the eigenvectors $\mathbf{I}_n$ do not change with the surface resistivity and only the eigenvalues have to be rescaled with R_{s}. Formula (4.2) can be simplified using

$$\text{eig}(\mathbf{R}_{\text{r}}, \mathbf{\Psi}) = \text{eig}(\mathbf{S}\mathbf{\Upsilon}^{-1}\mathbf{\Upsilon}^{-\text{H}}\mathbf{S}^{\text{H}}) = \text{svd}(\mathbf{S}\mathbf{\Upsilon}^{-1})^2, \tag{4.3}$$

where we also used the factorization $\mathbf{R}_{\text{r}} = \mathbf{S}^{\text{H}}\mathbf{S}$ based on the spherical mode matrix $\mathbf{S}$, [55], see Appendix A, and a Cholesky factorization $\mathbf{\Psi} = \mathbf{\Upsilon}^{\text{H}}\mathbf{\Upsilon}$ to reduce the computational burden. The radiation modes in (4.2) produce an expansion in modes with orthogonal far fields and increasing dissipation factors. They also appear in the analysis of the eigenvalue problems for the radiation operator [51] and for MIMO capacity problems. Notice, that for a spherical shell they form a set of properly scaled spherical harmonics.

Radiation modes (4.2) are evaluated for a rectangular plate of side aspect ratio 2 : 1 and electrical sizes $ka \in \{0.1, 0.32, 1, 3.2, 10\}$ and the normalized eigenvalues $\varrho_n R_{\text{s}}$ are depicted in Fig. 10. The low-order modes are emphasized in the inset, where

it is seen that the modes appear in groups with similar amplitudes for small ka. This is confirmed via spherical mode expansion, see Appendix F, for which the rectangular plate supports only half of the spherical modes, *e.g.*, x- and y- electrical and z-directed magnetic dipole modes. This characteristic is most emphasized for electrically small structures and the increasing cost of higher order modes vanishes with increasing electrical size, *e.g.*, the first ten modes for $ka = 3.2$ differ only in a factor of ten compared to 10^5 for $ka = 0.32$.

5 Conclusion

Maximum gain and effective area for arbitrarily shaped antenna regions are formulated as quadratically constrained quadratic programs (QCQP) which are effectively solved as low-rank eigenvalue problems. The approach is general and includes constraints on self-resonance and parasitic objects, such as reflectors and ground planes. Radiation modes are used to interpret the results and simplify the numerical solution of the optimization problems.

The results are illustrated for a variety of shapes, electrical sizes ranging from subwavelength objects to objects hundreds of wavelengths long, and resistivities covering a wide range from superconductivity to lossy resistive sheets. Plotting the maximal gain versus electrical size reveals three regions. Dipole and Huygens sources dominate in the electrically small region, where the gain depends strongly on the resistivity and whether self-resonance is enforced or not. The effect of self-resonance diminishes as the electrical size approaches a wavelength. End-fire radiation dominates over broadside radiation for objects of wavelength sizes. This changes in the limit of electrically large objects where the effective area is proportional to geometrical cross-section and broadside radiation dominates over endfire radiation.

Superdirectivity is analyzed from the perspective of determining the trade-off between directivity and efficiency. Here, it is shown that the problem of maximum gain for a given resistivity is solved by the same eigenvalue problem as minimum dissipation factor for a given directivity. Moreover, numerical results suggest that the increase in the dissipation and Q-factor are similar for superdirectivity.

The results presented in this paper are of general interest as they can be utilized to evaluate the actual performance of designed and manufactured antennas and scatterers with respect to the fundamental bounds. Together with the previously published bounds on Q-factor and radiation efficiency, this work completes the rigorous study of electrically small antenna limits and extends the fundamental bounds towards the electrical large antennas. Understanding of fundamental bounds and knowledge in optimal currents reopen a call for optimal antenna designs.

Acknowledgements

This work was supported by the Swedish Foundation for Strategic Research (SSF) grant no. AM13-0011. The work of M. Capek was supported by the Ministry of Education, Youth and Sports through the project CZ.02.2.69/0.0/0.0/16_027/0008465.

Appendix A Matrix Representation of Used Operators

The matrices used in the optimization problems are constructed by expansion of the current density $\boldsymbol{J}(\boldsymbol{r})$ according (2.3) for $\boldsymbol{r} \in \Omega$.

The far-field matrix for direction $\hat{\boldsymbol{r}}$ reads [17]

$$\mathbf{F} = \begin{pmatrix} \mathbf{F}_{\hat{\boldsymbol{e}}} \\ \mathbf{F}_{\hat{\boldsymbol{h}}} \end{pmatrix}, \tag{A.1}$$

where $\hat{\boldsymbol{e}} = \hat{\boldsymbol{h}} \times \hat{\boldsymbol{r}}$ and $\hat{\boldsymbol{h}} = \hat{\boldsymbol{r}} \times \hat{\boldsymbol{e}}$ denote two orthogonal polarizations with elements

$$F_{\hat{\boldsymbol{e}},n} = \frac{-\mathrm{j}k\sqrt{Z_0}}{4\pi} \int_{\Omega} \hat{\boldsymbol{e}} \cdot \boldsymbol{\psi}_n(\boldsymbol{r}_1) \mathrm{e}^{\mathrm{j}k\boldsymbol{r}_1 \cdot \hat{\boldsymbol{r}}} \, \mathrm{dS}_1, \tag{A.2}$$

and similarly for $\mathbf{F}_{\hat{\boldsymbol{h}}}$.

The radiation resistance matrix $\mathbf{R}_\mathrm{r}$ and reactance matrix $\mathbf{X}$ form the MoM electric field integral equation (EFIE) impedance matrix $\mathbf{Z} = \mathbf{R}_\mathrm{r} + \mathrm{j}\mathbf{X}$ of a structure modeled as perfect electric conductor (PEC) [27].

The ohmic loss matrix $\mathbf{R}_\Omega = R_\mathrm{s}\boldsymbol{\Psi}$ for a region with a homogeneous surface resistivity, *i.e.*, R_s, is given by the Gram matrix [28], defined as

$$\Psi_{mn} = \int_{\Omega} \boldsymbol{\psi}_m(\boldsymbol{r}) \cdot \boldsymbol{\psi}_n(\boldsymbol{r}) \, \mathrm{dS}. \tag{A.3}$$

The expansion matrix between basis functions used and spherical waves reads [55]

$$S_{\upsilon n} = k\sqrt{Z_0} \int_{\Omega} \mathbf{u}_\upsilon^{(1)}(k\boldsymbol{r}) \cdot \boldsymbol{\psi}_n(\boldsymbol{r}) \, \mathrm{dS}\,, \tag{A.4}$$

where $\mathbf{u}_\upsilon^{(1)}$ denotes the regular spherical vector waves with index υ [37]. The matrix $\mathbf{S}$ is a low-rank factorization of the radiation resistance matrix $\mathbf{R}_\mathrm{r} = \mathbf{S}^\mathrm{H}\mathbf{S}$.

Appendix B QCQP

Maximum gain for self-resonant currents is determined from a QCQP [8, 46] of the form (2.16)

$$\begin{aligned} \text{maximize} \quad & \mathbf{I}^\mathrm{H}\mathbf{U}\mathbf{I} \\ \text{subject to} \quad & \mathbf{I}^\mathrm{H}\mathbf{R}\mathbf{I} = 1 \\ & \mathbf{I}^\mathrm{H}\mathbf{X}\mathbf{I} = 0, \end{aligned} \tag{B.1}$$

where $\mathbf{U} = \mathbf{U}^\mathrm{H} \succeq \mathbf{0}$, $\mathbf{R} = \mathbf{R}^\mathrm{T} \succeq \mathbf{0}$, and $\mathbf{X} = \mathbf{X}^\mathrm{T}$ being indefinite. This formulation can be relaxed to a dual problem

$$\begin{aligned} \underset{\nu}{\text{minimize}} \; \underset{\mathbf{I}}{\text{maximize}} \quad & \mathbf{I}^\mathrm{H}\mathbf{U}\mathbf{I}, \\ \text{subject to} \quad & \mathbf{I}^\mathrm{H}(\nu\mathbf{X} + \mathbf{R})\mathbf{I} = 1, \end{aligned} \tag{B.2}$$

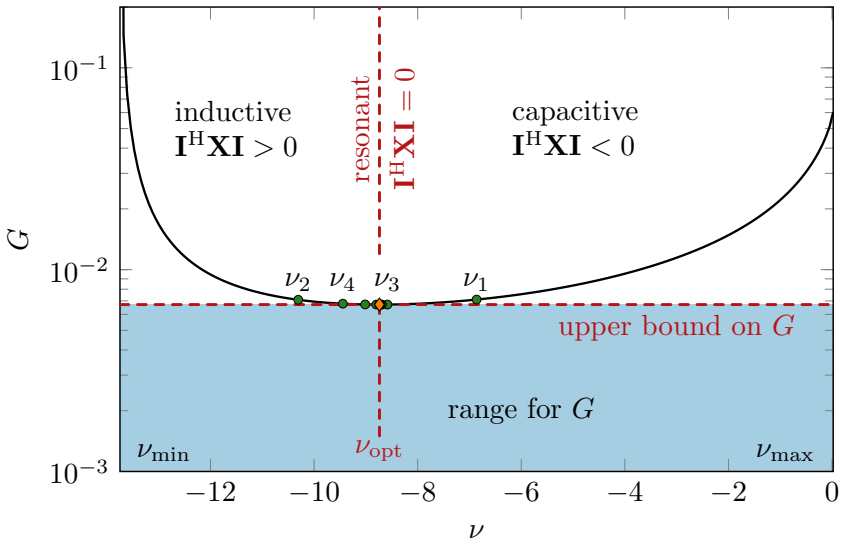

Figure 11: Solution of the QCQP (B.1) using the dual formulation (B.3). The range $[\nu_{\min}, \nu_{\max}] \approx [-13.7, 0.02]$ for the dual parameter ν is determined in Appendix E by (E.6) and the optimal parameter value $\nu_{\mathrm{opt}} \approx -8.74$ is determined from the sequence ν_n, $n = \{1, 2, \ldots\}$ using the bisection algorithm [43].

analogously to the analysis in Section 2.2 with the solution

$$\underset{\nu}{\text{minimize}} \max \operatorname{eig}(\mathbf{U}, \nu\mathbf{X} + \mathbf{R}). \tag{B.3}$$

The range $\nu \in [\nu_{\min}, \nu_{\max}]$ is restricted such that

$$\nu\mathbf{X} + \mathbf{R} \succeq \mathbf{0}, \tag{B.4}$$

and an efficient procedure to find $\nu_{\min}$ and $\nu_{\max}$ is outlined in Appendix E.

The minimization problem (B.3) is solved iteratively using a line-search algorithm, *e.g.*, the bisection algorithm [43], where also the derivative (2.19) is used, see Fig. 11 showing the optimization setup. Note that the Newton algorithm [8] can be used if the Hessian is evaluated as, *e.g.*, in the case with partial gain [17].

The explicit form of the derivative (2.19) also shows that the derivative is zero for the optimal value ν_{opt} if the eigenvalue depends continuously on ν as the derivative changes sign around ν_{opt}. Hence, the solution to (B.3), $\mathbf{I}_{\mathrm{opt}}$, at the extreme point ν_{opt} is self resonant $\mathbf{I}_{\mathrm{opt}}^{\mathrm{H}}\mathbf{X}\mathbf{I}_{\mathrm{opt}} = 0$ and satisfies the second constraint in the QCQP (B.1). This implies that the duality gap is zero and that the QCQP (B.1) is solved by its dual (B.3). Moreover, non-degenerate eigenvalues depend continuously on parameters [34] so the problem is solved for this case. For a treatment of modal degeneracies and other implementation issues, see Appendix D.

Appendix C Alternative Solutions to QCQP

The Lagrangian dual [8] is convex and offers an alternative approach to solve the QCQP (B.1). It is given by the semidefinite program (SDP)

$$\begin{aligned} \text{minimize} \quad & \mu, \\ \text{subject to} \quad & -\mathbf{U} + \nu\mathbf{X} + \mu\mathbf{R} \succeq \mathbf{0}, \\ & \mu \geq 0, \quad \nu \in \mathbb{R}, \end{aligned} \tag{C.1}$$

which can be solved efficiently [8]. The semidefinite constraint in the Lagrangian dual (C.1) can be written

$$\mathbf{I}^{\mathrm{H}}(\nu\mathbf{X} + \mu\mathbf{R})\mathbf{I} = \mu\mathbf{I}^{\mathrm{H}}(\nu_1\mathbf{X} + \mathbf{R})\mathbf{I} \geq \mathbf{I}^{\mathrm{H}}\mathbf{U}\mathbf{I} \tag{C.2}$$

for all currents $\mathbf{I}$ and $\nu_1 = \nu/\mu$. Here, it is seen that $\nu_1\mathbf{X} + \mathbf{R} \succeq \mathbf{0}$ and

$$\mu \geq \frac{\mathbf{I}^{\mathrm{H}}\mathbf{U}\mathbf{I}}{\mathbf{I}^{\mathrm{H}}(\nu_1\mathbf{X} + \mathbf{R})\mathbf{I}} \geq \min_{\nu_1} \max \mathrm{eig}(\mathbf{U}, \nu_1\mathbf{X} + \mathbf{R}) \tag{C.3}$$

and hence the solution of the Lagrangian dual in (C.1) is similar to the solution (B.3) of the relaxation (B.2). The only difference is in the range for ν_1 that is a subset of (E.6) due to the $\mathbf{I}^{\mathrm{H}}\mathbf{U}\mathbf{I}$ term in the right-hand side of (C.2). However, self-resonant solutions of (3.4) satisfies (C.2). Semidefinite relaxation is another standard relaxation technique [8] for the QCQP (B.1).

Appendix D Numerical Evaluation of QCQP

In this paper, the implementation is as follows. We use the eigenvalue problem (B.2) together with the factorization $\mathbf{U} = \mathbf{F}^{\mathrm{H}}\mathbf{F}$ due to its simplicity and computational efficiency. The computational complexity is dominated by the solution of the linear system $(\nu\mathbf{X} + \mathbf{R})^{-1}\mathbf{F}^{\mathrm{H}}$ which requires of the order N^3 operations for direct solvers, where N is the number of basis functions, *cf.* (2.3). Here, we also note that the additional computational cost of using multiple directions $\mathbf{F}$ is negligible. For electrically large structures we use iterative algorithms to solve the linear system [50]. The rectangle in Fig. 4 was, *e.g.*, solved iteratively using a matrix-free FFT-based formulation [10] using $N \approx 4.2 \cdot 10^6$ unknowns for $ka \approx 10^3$. The fast multipole method (FMM) and similar techniques can also be used [10] to reduce the computational burden.

Whenever possible, symmetries are used to simplify the solution by separating the eigenvalue problem into orthogonal subspaces which are solved separately and combined analytically [15]. This reformulates the optimization problems into block diagonal form, where each block corresponds to a subspace. The problem is further simplified for cases where some of the subspaces do not contribute to the radiation intensity in the considered direction as, *e.g.*, for radiation in the normal direction $\hat{\boldsymbol{k}} = \hat{\boldsymbol{z}}$ for the rectangle in Fig. 4, where currents with odd inversion symmetry $\boldsymbol{J}(\boldsymbol{r}) = -\boldsymbol{J}(-\boldsymbol{r})$ do not contribute and similarly for the cylinder in Fig. 5

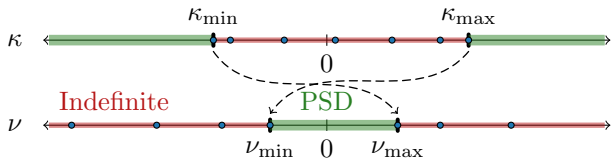

Figure 12: Determination of the range of ν : $\nu\mathbf{X}+\mathbf{R} \succeq \mathbf{0}$; eigenvalues κ are solutions to $\mathbf{XI} = \kappa\mathbf{RI}$.

where azimuthal Fourier indices $|m| \neq 1$ do not contribute. For these cases, the currents in the non-contributing subspace can only be used to tune the currents into self resonance. Hence, they are quiescent in the externally tuned case (2.8) and determined by the eigenvectors associated with the largest eigenvalues of the eigenvalue problems in (2.20), where the matrices $\mathbf{X}, \mathbf{R}_{\mathrm{r}}$, and $\mathbf{R}_{\Omega}$ are restricted to the non-contributing subspace.

Expansion in radiation modes (4.2) is also useful in the solution of the maximum gain optimization problem (2.13), which contains the solution of the linear system $(\mathbf{R}_{\mathrm{r}} + R_{\mathrm{s}}\boldsymbol{\Psi})^{-1}\mathbf{F}^{\mathrm{H}}$ and often is solved for many values of R_{s} as in Section 3. Using $\mathbf{R}_{\mathrm{r}} = \mathbf{S}^{\mathrm{H}}\mathbf{S}$ and $\mathbf{R}_{\Omega} = R_{\mathrm{s}}\boldsymbol{\Upsilon}^{\mathrm{H}}\boldsymbol{\Upsilon}$ together with the singular value decomposition (SVD) $\mathbf{U}\boldsymbol{\Sigma}\mathbf{V}^{\mathrm{H}} = \mathbf{S}\boldsymbol{\Upsilon}^{-1}$ reduces the inversion of the linear system to inversion of a diagonal matrix, *i.e.*,

$$\begin{aligned}(\mathbf{R}_{\mathrm{r}} + \mathbf{R}_{\Omega})^{-1} &= (\mathbf{S}^{\mathrm{H}}\mathbf{S} + R_{\mathrm{s}}\boldsymbol{\Upsilon}^{\mathrm{H}}\boldsymbol{\Upsilon})^{-1} = \boldsymbol{\Upsilon}^{-1}(\boldsymbol{\Upsilon}^{-\mathrm{H}}\mathbf{S}^{\mathrm{H}}\mathbf{S}\boldsymbol{\Upsilon}^{-1} + R_{\mathrm{s}}\mathbf{1})^{-1}\boldsymbol{\Upsilon}^{-\mathrm{H}} \\ &= \boldsymbol{\Upsilon}^{-1}(\mathbf{V}^{-\mathrm{H}}\boldsymbol{\Sigma}^{\mathrm{H}}\boldsymbol{\Sigma}\mathbf{V}^{\mathrm{H}} + R_{\mathrm{s}}\mathbf{1})^{-1}\boldsymbol{\Upsilon}^{-\mathrm{H}} = \boldsymbol{\Upsilon}^{-1}\mathbf{V}(\boldsymbol{\Sigma}^{\mathrm{H}}\boldsymbol{\Sigma} + R_{\mathrm{s}}\mathbf{1})^{-1}\mathbf{V}^{\mathrm{H}}\boldsymbol{\Upsilon}^{-\mathrm{H}}, \quad \text{(D.1)}\end{aligned}$$

where $\mathbf{1}$ denotes the identity matrix. The computational cost of sweeping the maximum gain versus R_{s} is hence traded to computation of the SVD of $\mathbf{S}\boldsymbol{\Upsilon}^{-1}$ that only requires $N_{\mathrm{s}}^2 N + N^2$ operations, where N_{s} denotes the number of spherical modes. Note, that we also use that matrix $\boldsymbol{\Psi}$ is a sparse matrix with approximately $3N$ non-zero elements that reduces the computational cost to compute $\boldsymbol{\Upsilon}$.

Appendix E Determination of $\nu_{\min}$ and $\nu_{\max}$

The task here is to find a range of ν, delimited by $\nu_{\min}$ and $\nu_{\max}$, such that (B.4) holds, $\mathbf{R} = \mathbf{R}^{\mathrm{T}} \succeq \mathbf{0}$, and $\mathbf{X} = \mathbf{X}^{\mathrm{T}}$ is indefinite. Equivalently, we can state that

$$\mathbf{I}^{\mathrm{H}}(\nu\mathbf{X} + \mathbf{R})\mathbf{I} \geq 0 \quad \forall \mathbf{I} \tag{E.1}$$

which can be reformulated to the Rayleigh quotient

$$\nu\frac{\mathbf{I}^{\mathrm{H}}\mathbf{X}\mathbf{I}}{\mathbf{I}^{\mathrm{H}}\mathbf{R}\mathbf{I}} \geq -1 \quad \forall \mathbf{I}. \tag{E.2}$$

First, consider the case with $\nu > 0$, for which the Rayleigh quotient satisfies

$$\frac{\mathbf{I}^{\mathrm{H}}\mathbf{X}\mathbf{I}}{\mathbf{I}^{\mathrm{H}}\mathbf{R}\mathbf{I}} \geq \min_{\mathbf{I}}\frac{\mathbf{I}^{\mathrm{H}}\mathbf{X}\mathbf{I}}{\mathbf{I}^{\mathrm{H}}\mathbf{R}\mathbf{I}} = \min \mathrm{eig}(\mathbf{X}, \mathbf{R}) = \kappa_{\min} \geq \frac{-1}{\nu} \tag{E.3}$$

that implies the upper limit of the interval

$$\nu \leq \nu_{\max} = \frac{-1}{\kappa_{\min}}, \tag{E.4}$$

where $\kappa_{\min}$ is the smallest eigenvalue, see Fig. 12.

Second, consider the case $\nu < 0$. Analogously to (E.3) we get

$$\frac{\mathbf{I}^{\mathrm{H}}\mathbf{X}\mathbf{I}}{\mathbf{I}^{\mathrm{H}}\mathbf{R}\mathbf{I}} \leq \max_{\mathbf{I}} \frac{\mathbf{I}^{\mathrm{H}}\mathbf{X}\mathbf{I}}{\mathbf{I}^{\mathrm{H}}\mathbf{R}\mathbf{I}} = \max \mathrm{eig}(\mathbf{X}, \mathbf{R}) = \kappa_{\max} = \frac{-1}{\nu} \tag{E.5}$$

and the range is given by (E.4) and (E.5) as

$$\frac{-1}{\kappa_{\max}} = \nu_{\min} \leq \nu \leq \nu_{\max} = \frac{-1}{\kappa_{\min}}. \tag{E.6}$$

Appendix F Maximum Gain for a Sphere

The optimization problems (2.8) and (2.16) are solved analytically for spherical structures using spherical waves [37]. The matrices in the eigenvalue problems (2.13) and (2.18) are diagonalized for spherical modes offering closed-form solutions of the eigenvalue problems. The radiation resistance and ohmic loss matrices have elements $(ka\,\mathrm{R}_{l\tau}^{(1)}(ka))^2$ and R_{s}, respectively, giving normalized dissipation factors $\delta_{l\tau}/R_{\mathrm{s}} = (ka\,\mathrm{R}_{l\tau}^{(1)}(ka))^{-2}$, where l is the order of the spherical mode, τ the TE or TM type, and $\mathrm{R}_{l\tau}^{(p)}$ radial functions [20]. Radiation dominates for modes with $(ka\,\mathrm{R}_{l\tau}^{(1)}(ka))^2 > R_{\mathrm{s}}$. This resembles (4.1) with the observation that the radial functions are negligible for $ka \ll l$.

The directivity associated with the maximum gain and effective area in Fig. 1 is depicted in Fig. 13. The directivity increases stepwise as additional modes are included. In the electrically small limit, the self-resonant case combines electric and magnetic dipoles to form a Huygens source with directivity $D = 3$. The radiation efficiency is, however, low as seen in the much lower gain in Fig. 1. Inclusion of quadrupole modes increases the directivity to $D = 8$ as seen by (4.1) for $L = 2$. The externally tuned case starts at $D = 3/2$, where the radiation is caused by a sole electric dipole. It increases to $D = 11/2$ when the magnetic dipole and electric quadrupole starts to contribute. This stepwise increase is explained by the lower losses for the TM modes, see Fig. 14, causing the modes to appear in order as $\{\mathrm{TM}_1\}$, $\{\mathrm{TM}_2, \mathrm{TE}_1\}$, $\{\mathrm{TM}_3, \mathrm{TE}_2\}$ giving directivity $D = L^2 + L - 1/2$ as compared with (4.1).

Appendix G Self-Resonant and Tuned Cases

The large difference between the gain (the effective area) for the externally tuned and self-resonant cases for electrically small structures originates in much higher dissipation factor for the loop current forming the TE dipole mode than for the charge separation producing the TM dipole mode [15, 30, 31, 48, 56]. The difference

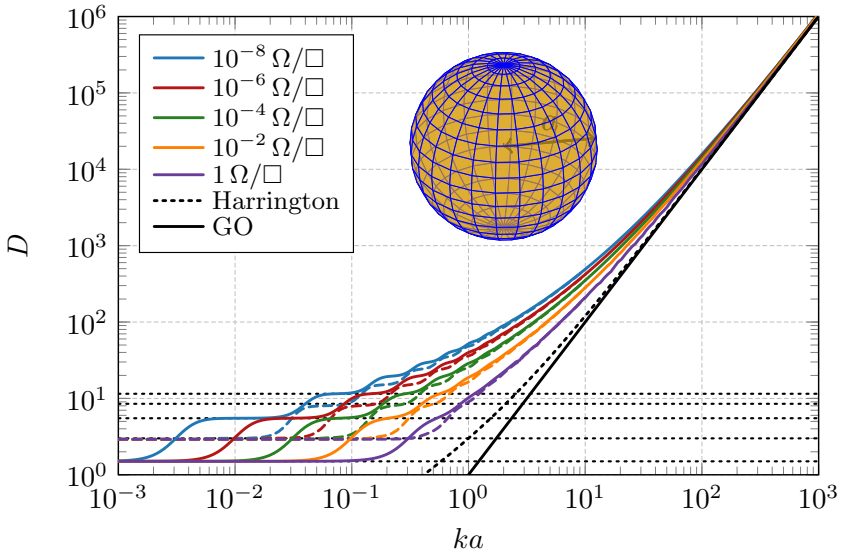

Figure 13: Resulting directivity from the maximum gain for a spherical shell with surface resistivity $R_\mathrm{s} \in \{10^{-n}\}\,\Omega/\square$ for $n = \{0, 2, 4, 6, 8\}$ in Fig. 1. Dotted lines depicts directivities $D \in \{3/2, 3, 11/2, 8, 23/2\}$ associated with the lowest order modes.

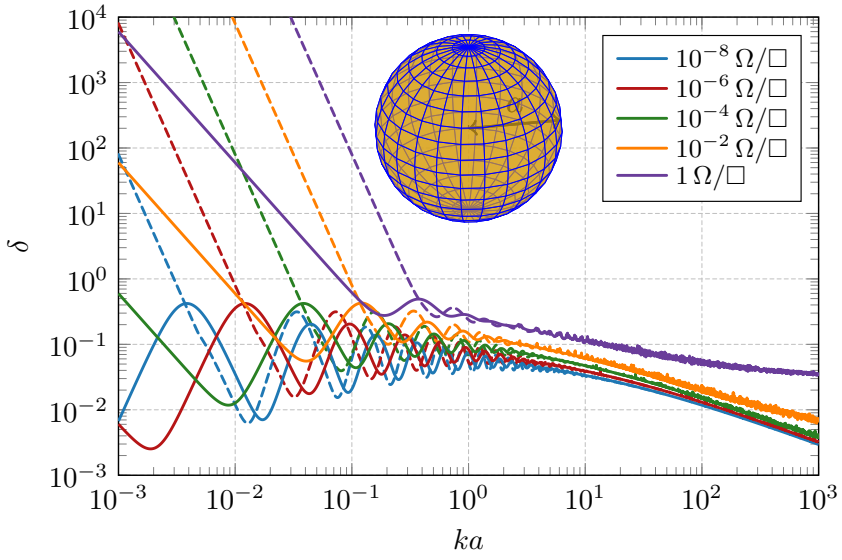

Figure 14: Resulting dissipation factor from the maximum gain for a spherical shell with surface resistivity $R_\mathrm{s} \in \{10^{-n}\}\,\Omega/\square$ for $n = \{0, 2, 4, 6, 8\}$ in Fig. 1.

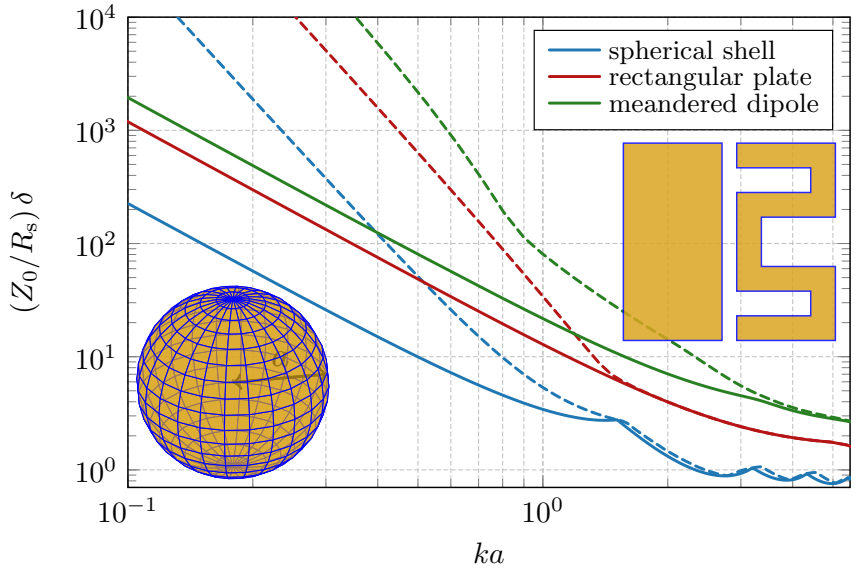

Figure 15: Minimum dissipation factors for a spherical shell (blue lines), a rectangular plate (red lines), and a meanderline (green lines) are depicted both for externally tuned (solid lines) and self-resonant (dashed lines) currents.

reduces as the electrical size increases and is negligible for the electrically large structures. The minimum dissipation factor for the two cases can be used as an estimate of the size when the self-resonance condition becomes irrelevant, which is demonstrated in Fig. 15 for examples of a spherical shell, a rectangular plate, and a meanderline.

References

[1] E. E. Altshuler, T. H. O'Donnell, A. D. Yaghjian, and S. R. Best. "A monopole superdirective array". *IEEE Trans. Antennas Propag.* 53 (8) (2005): pp. 2653–2661.

[2] A. Arbabi and S. Safavi-Naeini. "Maximum gain of a lossy antenna". *IEEE Trans. Antennas Propag.* 60 (1) (2012): pp. 2–7.

[3] S. Arslanagić and R. W. Ziolkowski. "Highly subwavelength, superdirective cylindrical nanoantenna". *Physical Review Letters* 120 (23) (2018).

[4] C. A. Balanis. "Advanced Engineering Electromagnetics". John Wiley & Sons, 2012.

[5] A. Bloch, R. Medhurst, and S. Pool. "A new approach to the design of superdirective aerial arrays". *Proc. IEE* 100 (67) (1953): pp. 303–314.

[6] C. F. Bohren. "How can a particle absorb more than the light incident on it?" *American Journal of Physics* 51 (4) (1998): pp. 323–327.

[7] C. Bouwkamp and N. De Bruijn. "The problem of optimum antenna current distribution". *Philips Res. Rep* 1 (2) (1945): pp. 135–158.

[8] S. P. Boyd and L. Vandenberghe. "Convex Optimization". Cambridge Univ. Pr., 2004.

[9] M. Capek, M. Gustafsson, and K. Schab. "Minimization of antenna quality factor". *IEEE Trans. Antennas Propag.* 65 (8) (2017): pp. 4115–4123.

[10] W. C. Chew, E Michielssen, J. Song, and J. Jin. "Fast and Efficient Algorithms in Computational Electromagnetics". Artech House, Inc., 2001.

[11] J. Diao and K. F. Warnick. "Practical superdirectivity with resonant screened apertures motivated by a poynting streamlines analysis". *IEEE Trans. Antennas Propag.* 66 (1) (2018): pp. 432–437.

[12] C. Ehrenborg and M. Gustafsson. "Fundamental bounds on MIMO antennas". *IEEE Antennas Wireless Propag. Lett.* 17 (1) (2018): pp. 21–24.

[13] R. S. Elliott. "Antenna Theory and Design". IEEE Press, 2003.

[14] N. Engheta and R. W. Ziolkowski. "Metamaterials: physics and engineering explorations". John Wiley & Sons, 2006.

[15] M. Gustafsson, M. Capek, and K. Schab. *Trade-off Between Antenna Efficiency and Q-Factor*. Tech. rep. LUTEDX/(TEAT-7260)/1–11/(2017). Lund University, 2017.

[16] M. Gustafsson and S. Nordebo. "Optimal antenna currents for Q, superdirectivity, and radiation patterns using convex optimization". *IEEE Trans. Antennas Propag.* 61 (3) (2013): pp. 1109–1118.

[17] M. Gustafsson, D. Tayli, C. Ehrenborg, M. Cismasu, and S. Nordebo. "Antenna current optimization using MATLAB and CVX". *FERMAT* 15 (5) (2016): pp. 1–29.

[18] M. Gustafsson. "Efficiency and Q for small antennas using Pareto optimality". In: *Antennas and Propagation Society International Symposium (APSURSI)*. IEEE. 2013, pp. 2203–2204.

[19] M. Gustafsson, D. Tayli, and M. Cismasu. "Physical bounds of antennas". In: *Handbook of Antenna Technologies*. Ed. by Z. N. Chen. Springer-Verlag, 2015, pp. 1–32.

[20] J. E. Hansen, ed. "Spherical Near-Field Antenna Measurements". IEE electromagnetic waves series 26. Peter Peregrinus Ltd., 1988.

[21] R. C. Hansen. "Fundamental limitations in antennas". *Proc. IEEE* 69 (2) (1981): pp. 170–182.

[22] R. C. Hansen. "Superconducting antennas". *IEEE Transactions on Aerospace and Electronic Systems* 26 (2) (1990): pp. 345–355.

[23] R. Harrington. "On the gain and beamwidth of directional antennas". *IEEE Trans. Antennas Propag.* 6 (3) (1958): pp. 219–225.

[24] R. F. Harrington. "Antenna excitation for maximum gain". *IEEE Trans. Antennas Propag.* 13 (6) (1965): pp. 896–903.

[25] R. F. Harrington. "Effect of antenna size on gain, bandwidth and efficiency". *Journal of Research of the National Bureau of Standards – D. Radio Propagation* 64D (1960): pp. 1–12.

[26] R. F. Harrington. "Time Harmonic Electromagnetic Fields". McGraw-Hill, 1961.

[27] R. F. Harrington. "Field Computation by Moment Methods". Macmillan, 1968.

[28] R. A. Horn and C. R. Johnson. "Topics in Matrix Analysis". Cambridge University Press, 1991.

[29] *IEEE Standard Definition of Terms for Antennas*. Antenna Standards Committee of the IEEE Antenna and Propagation Society. 1993.

[30] L Jelinek and M Capek. "Optimal currents on arbitrarily shaped surfaces". *IEEE Trans. Antennas Propag.* 65 (1) (2017): pp. 329–341.

[31] L. Jelinek, K. Schab, and M. Capek. "The radiation efficiency cost of resonance tuning". *IEEE Trans. Antennas Propag.* 66 (12) (2017): pp. 6716–6723.

[32] B. L. G. Jonsson, S. Shi, L. Wang, F. Ferrero, and L. Lizzi. "On methods to determine bounds on the Q-factor for a given directivity". *IEEE Trans. Antennas Propag.* 65 (11) (2017): pp. 5686–5696.

[33] A. Karlsson. "On the efficiency and gain of antennas". *Progress In Electromagnetics Research* 136 (2013): pp. 479–494.

[34] T. Kato. "Perturbation Theory for Linear Operators". Springer-Verlag, 1980.

[35] P.-S. Kildal, E. Martini, and S. Maci. "Degrees of freedom and maximum directivity of antennas: a bound on maximum directivity of nonsuperreactive antennas". *IEEE Antennas and Propagation Magazine* 59 (4) (2017): pp. 16–25.

[36] O. Kim, S. Pivnenko, and O. Breinbjerg. "Superdirective magnetic dipole array as a first-order probe for spherical near-field antenna measurements". *IEEE Trans. Antennas Propag.* 60 (10) (2012): pp. 4670–4676.

[37] G. Kristensson. "Scattering of Electromagnetic Waves by Obstacles". SciTech Publishing, an imprint of the IET, 2016.

[38] P. Lancaster. "On eigenvalues of matrices dependent on a parameter". *Numerische Mathematik* 6 (1) (1964): pp. 377–387.

[39] I. Liberal, I. Ederra, R. Gonzalo, and R. W. Ziolkowski. "Superbackscattering antenna arrays". *IEEE Trans. Antennas Propag.* 63 (5) (2015): pp. 2011–2021.

[40] I. Liberal, I. Ederra, R. Gonzalo, and R. W. Ziolkowski. "Upper bounds on scattering processes and metamaterial-inspired structures that reach them". *IEEE Trans. Antennas Propag.* 62 (12) (2014): pp. 6344–6353.

[41] D. Margetis, G. Fikioris, J. M. Myers, and T. T. Wu. "Highly directive current distributions: general theory". *Physical Review E* 58 (2) (1998): p. 2531.

[42] O. D. Miller, A. G. Polimeridis, M. H. Reid, C. W. Hsu, B. G. DeLacy, J. D. Joannopoulos, M. Soljačić, and S. G. Johnson. "Fundamental limits to optical response in absorptive systems". *Optics express* 24 (4) (2016): pp. 3329–3364.

[43] J. Nocedal and S. J. Wright. "Numerical Optimization". Operations Research and Financial Engineering. Springer-Verlag, 2006.

[44] C. W. Oseen. "Die einsteinsche nadelstichstrahlung und die maxwellschen gleichungen". *Annalen der Physik* 374 (19) (1922): pp. 202–204.

[45] H. Padamsee, J. Knobloch, and T. Hays. "RF Superconductivity for Accelerators". John Wiley & Sons, 1998.

[46] J. Park and S. Boyd. "General heuristics for nonconvex quadratically constrained quadratic programming". *arXiv preprint arXiv:1703.07870* (2017).

[47] H. Paul and R. Fischer. "Light absorption by a dipole". *Soviet Physics Uspekhi* 26 (10) (1983): pp. 923–926.

[48] C. Pfeiffer. "Fundamental efficiency limits for small metallic antennas". *IEEE Trans. Antennas Propag.* 65 (4) (2017): pp. 1642–1650.

[49] M. Pigeon, C. Delaveaud, L. Rudant, and K. Belmkaddem. "Miniature directive antennas". *International Journal of Microwave and Wireless Technologies* 6 (01) (2014): pp. 45–50.

[50] Y. Saad. "Iterative Methods for Sparse Linear Systems". PWS Publishing Company, 1996.

[51] K. R. Schab. "Modal analysis of radiation and energy storage mechanisms on conducting scatterers". PhD thesis. University of Illinois at Urbana-Champaign, 2016.

[52] E. Shamonina and L. Solymar. "Maximum directivity of arbitrary dipole arrays". *IET Microw. Antenna P.* 9 (2) (2015): pp. 101–107.

[53] S. Silver. "Microwave Antenna Theory and Design". Vol. 12. Radiation Laboratory Series. McGraw-Hill, 1949.

[54] C. Sohl, M. Gustafsson, and G. Kristensson. "Physical limitations on metamaterials: restrictions on scattering and absorption over a frequency interval". *J. Phys. D: Applied Phys.* 40 (2007): pp. 7146–7151.

[55] D. Tayli, M. Capek, L. Akrou, V. Losenicky, L. Jelinek, and M. Gustafsson. "Accurate and efficient evaluation of characteristic modes". *IEEE Trans. Antennas Propag.* 66 (12) (2018): pp. 7066–7075.

[56] H. L. Thal. "Radiation efficiency limits for elementary antenna shapes". *IEEE Trans. Antennas Propag.* 66 (5) (2018): pp. 2179 –2187.

[57] M Uzsoky and L Solymár. "Theory of super-directive linear arrays". *Acta physica Academiae Scientiarum Hungaricae* 6 (2) (1956): pp. 185–205.

[58] G. A. E. Vandenbosch. "Reactive energies, impedance, and Q factor of radiating structures". *IEEE Trans. Antennas Propag.* 58 (4) (2010): pp. 1112–1127.

[59] A. D. Yaghjian, T. H. O'Donnell, E. E. Altshuler, and S. R. Best. "Electrically small supergain end-fire arrays". *Radio Science* 43 (3) (2008): pp. 1–13.

[60] N. Yaru. "A note on super-gain antenna arrays". *Proceedings of the IRE* 39 (9) (1951): pp. 1081–1085.

[61] R. W. Ziolkowski. "Using Huygens multipole arrays to realize unidirectional needle-like radiation". *Physical Review X* 7 (3) (2017): p. 031017.